Version of Record: https://www.sciencedirect.com/science/article/pii/S0045793022001438
Manuscript_ff6e368f7605f930bc762c65b1bfbb73

Stochastic boundary condition effects on supersonic leading edge blowing

Francisco Lozano, Iman Rahbari, Guang Lin & Guillermo Paniagua

School of Mechanical Engineering, Purdue University, West Lafayette IN 47907, USA

The present manuscript studies the robustness of leading edge blowing for active control of the upstream bow shock and overall aerothermal characteristics of a supersonic airfoil subject to variability in the injection conditions. The injection boundary conditions were considered stochastic and their randomness was propagated to the flow topology and aerothermal quantities of interest by means of non-intrusive Polynomial Chaos Expansions. The evaluations needed to build these expansions were carried out via steady two-dimensional Reynolds-Averaged Navier Stokes simulations. Two different injection port sizes were considered, with the smallest promoting a Coanda effect that gives rise to non-symmetric flow topologies. The uncertain boundary conditions lead to significant variations in the flow topology, particularly at the injection exit and the bow shock position, with variations of up to 75 % of the nominal value. This study identifies the key operating conditions to ensure the optimal application of leading-edge injection for active control of supersonic airfoils.

Keywords: Supersonic flow, bow shock, flow control, Coanda, Polynomial Chaos.

1. Introduction

Leading edge bow shock waves are responsible for aerodynamic performance abatement, as well as severe thermo-mechanical loads [1], which determine the life of supersonic aerospace systems. Among the different shock topologies, the bow shock and its control is of particular interest as it appears in all cases where a two-dimensional (2D) or axi-symmetric body is immersed in a supersonic flow. Furthermore, it appears at the leading edge, the most critical point since it endures the maximum heat loads.

A detailed review of passive and active methodologies to control the bow shock is provided by Bushnell [3]. Uncertainty Quantification (UQ) aims at: identifying the sources of uncertainty, propagating their effect through the system and estimating their impact on the quantities of interest for a given application. Among different UQ tools, Polynomial Chaos Expansions (PCE) are widely used in computational fluid dynamics [4] [5]. Ahlfeld et al. [6] used Pade-Legendre polynomials to assess the effects of stochastic variables on the trailing edge injection of an airfoil geometry. This study was performed for a supersonic flow characterized by shock structures similar to the one considered in this manuscript.

The aim of the present manuscript is to use PCE to assess the robustness of the leading edge counterflowing jet under stochastic boundary conditions. The paper documents the impact of non-deterministic operating conditions on the flow topology and aerothermal performance of the airfoil on which the leading edge blowing is applied. The results obtained for two different leading edge injection geometries are discussed. Physical insight into the drag reduction mechanism created by leading-edge injection and a brief comparison between two different kinds of Polynomial Chaos Expansions were selected for this study.

2. Numerical approach

2.1 Computational domain

Flow simulations were carried out by solving 2D fully compressible steady Reynolds-Averaged Navier Stokes (RANS) equations using a Finite Volume Method (FVM) solver with the second-order upwind spatial discretization. The $k-\omega$ SST turbulence model was chosen to obtain the turbulence closure. The first grid location away from the wall was chosen such that $\Delta y^+ < 1$ throughout the airfoil surface, where $\Delta y^+ = \Delta y\, u_\tau/\nu_{wall}$ and $u_\tau = \sqrt{\tau_{wall}/\rho_{wall}}$. The grid sensitivity analysis, performed according to the procedure provided by Celik et al. [8], yielded grids with 605,459 and 598,600 cells for the cases with large and small injection slots, respectively. The solver validation study was performed against experimental results by Finley [2] for a counter-flowing jet applied at the leading edge of an aerodynamic body facing a supersonic flow and a satisfactory agreement was achieved [7].

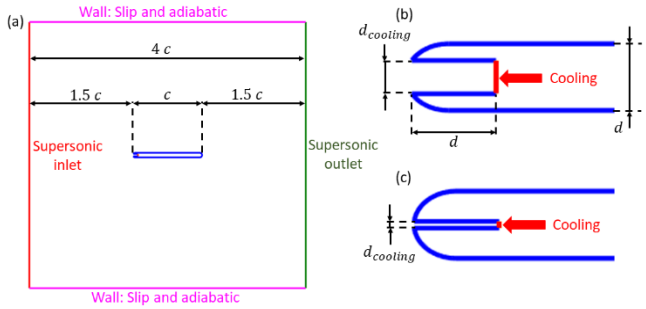

Figure 1: Computational domain (a) and leading edge close-up views for baseline cases with large (b) and narrow (c) leading edge injection slots.

The computational domain employed for these simulations is depicted in Figure 1. Graphic (a) shows the complete

computational domain and summarizes the main boundary conditions applied. Graphics (b) and (c) present close-up views of the leading edge injection geometries explored in this manuscript: the large injection slot (b) and the narrow one (c).

The main boundary conditions are summarized in Table 1. At the main-stream inlet, the total and static pressure and total temperature were imposed. Quantities at this location are labeled with subindex 1 and they result in a supersonic Mach number $M_1 = 1.98$. The main flow outlet is supersonic, and therefore, all quantities were extrapolated from the inside the domain and no extra condition was needed. The airfoil wall was considered isothermal, with the constant wall temperature T_{wall} given in Table 1.

Table 1: Main flow boundary conditions.

$p_{01}\ [Pa]$	757,749
$T_{01}\ [K]$	2743
$p_1\ [Pa]$	100,560
$T_{wall}\ [K]$	1000

2.2 Steady blowing through a large port: $d_{cooling}/d = 0.5$

The baseline configurations considered in this study are first introduced by Lozano and Paniagua [7]. Injecting a jet opposed to a supersonic free stream at the leading-edge, can create different injection regimes: subsonic and supersonic injections. Figure 2 (a) shows the Mach number contour and main flow features for a subsonic injection. The bow shock (labeled as G), causes a sudden flow deceleration. Downstream, the flow becomes subsonic. F designates the interface which separates the cold leading edge injection fluid from the mainstream. F represents a thermal shield, protecting the airfoil from the supersonic mainstream. The saddle point (E) corresponds to the point where the hot mainstream and the cold blowing one collide. The hot mainstream flow bifurcates at this point, turning above or below the airfoil.

In the subsonic case, the cooling jet leaves the injection cavity with a Mach number below 1 and it decelerates until it finds the saddle point in the subsonic region downstream of the bow shock. As it leaves the circular part defining the leading-edge geometry, the flow expands and the Mach number increases from slightly above unity to higher supersonic values through an expansion fan. Then, it continues its path downstream following the free stream.

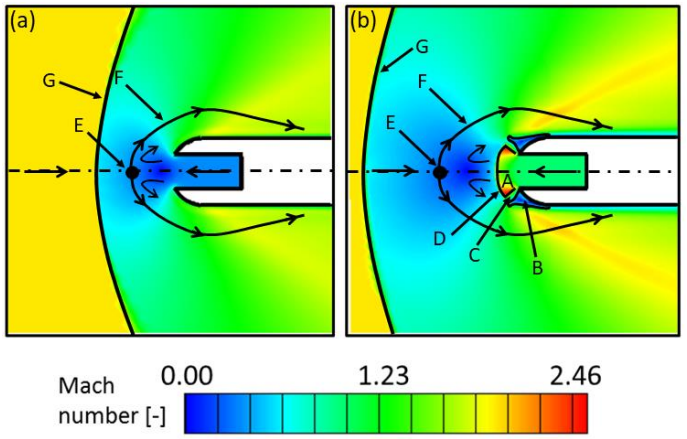

Figure 2: Mach number contours and flow topology schematics for a subsonic injection with leading-edge injection total pressure and temperature ratios $\boldsymbol{p_{0\,cooling}/p_{01} = 0.739}$ and $\boldsymbol{T_{0\,cooling}/T_{01} = 0.5}$ (a) and a supersonic injection with $\boldsymbol{p_{0\,cooling}/p_{01} = 0.900}$ and $\boldsymbol{T_{0\,cooling}/T_{01} = 0.5}$ (b).

Figure 2 (b) present the same quantity for a sample supersonic injection with $p_{0\,cooling}/p_{01} = 0.900$ and $T_{0c}/T_{01} = 0.5$. This configuration shares the features labeled as E, F and G with the subsonic one. However, a more complex flow topology arises, adding some new ones. In the supersonic injection configuration, as the cooling jet leaves the injection cavity at $M = 1$, it expands to the supersonic regime creating an artificial nozzle (A). This supersonic region is bounded on its upstream part by a terminal shock (D), which separates it from the subsonic region extending all the way to the bow shock and containing the saddle point. On both sides of the injection, next to the airfoil's surface, two separation zones appear (B). The separation zones are divided from the central supersonic expansion region by shear layers (C) formed due to the large momentum gradient between regions A and B. Furthermore, on n the sides of the separation zones, the expansion fans accelerating the flow around the leading edge can be observed. The higher momentum of the cooling jet also conveys a higher intensity to this expansion processes with respect to the subsonic case, reaching higher Mach numbers downstream.

2.3 Steady blowing through a small port: $d_{cooling}/d = 0.1$

When reducing the leading edge injection cavity width to $d_{cooling}/d = 0.1$, see Figure 1 (c), a Coanda effect appears for certain blowing boundary conditions. This phenomenon makes the leading edge flow topology non-symmetric in spite of the problem setup being completely symmetric. An example of this Coanda effect can be appreciated in the Mach number contour depicted in Figure 3 (a). This Coanda effect was already documented in the literature for other configurations involving sudden expansions, e.g. for trailing edge injection [9]. It is associated with a bifurcation phenomenon which makes various flow solutions possible for the same boundary conditions. The flow converges to one of them and remains there in a steady

fashion. Some authors pointed out a critical Reynolds number [10][11], as well as the expansion ratio between the channel and the main flow [12]. as the driving parameters dictating the appearance of the bifurcation phenomena leading to the Coanda effect. For the leading edge configuration investigated herein, a parametric study determined the leading edge injection Mach number to be the critical factor [7], where the low injection Mach numbers promote the Coanda effect.

Given the fundamentally different flow topologies found in the cases presented in Figure 2 and Figure 3, two different baseline cases were considered in the present study. The first one, referred to as the *Symmetric case*, hereafter, corresponds to a large injection cavity with ($d_{cooling}/d = 0.5$). The second one corresponds to a small injection cavity ($d_{cooling}/d = 0.1$), where the Coanda effect is expected, therefore called *Coanda case* hereon.

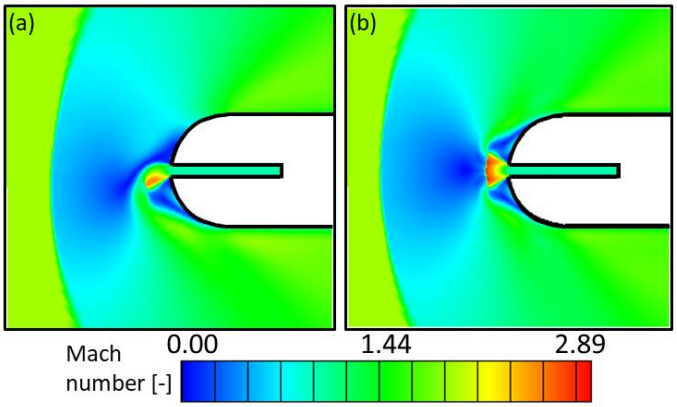

Figure 3: Mach number contours for a supersonic injection with the Coanda effect. The leading-edge injection total pressure and temperature ratios are $\boldsymbol{p_{0\,cooling}/p_{01} = 1.5}$ and $\boldsymbol{T_{0\,cooling}/T_{01} = 0.5}$ (a) and a supersonic symmetric injection with $\boldsymbol{p_{0\,cooling}/p_{01} = 2.0}$ and $\boldsymbol{T_{0\,cooling}/T_{01} = 0.5}$ (b).

2.4 Polynomial chaos expansions for uncertainty propagation

The approach to evaluating the effect of stochastic boundary conditions is based on non-intrusive Polynomial Chaos Expansions (PCE). The uncertain parameters are the boundary conditions imposed at the leading-edge injection of the supersonic airfoil: (1) cooling total pressure ($p_{0\,cooling}$), (2) total temperature ($T_{0\,cooling}$) and (3) turbulence intensity ($Tu_{cooling}$). These three random variables were assumed independent and uniformly distributed with the ranges shown in Table 2. These quantities composed the input variables vector, X. The quantities of interest (Y) dependence on the input variables can be expressed as:

$$Y^k = Y^k(X_1, X_2, X_3) \qquad (1)$$

where $k = 1, 2, 3, \ldots n_{\mathrm{QoI}}$. In the present study, the quantities of interest (n_{QoI}) are the Mach number at different positions around the leading edge, static pressure, wall shear stress and heat flux values on the airfoil's surface as well as the horizontal distance between the leading edge and the bow shock. Each of the random input variables are defined in an interval according to their characteristic values.

Table 2: Stochastic boundary conditions distributions.

	$\frac{p_{0c}}{p_{01}}$ [−]	$\frac{T_{0c}}{T_{01}}$ [−]	Tu_c [%]
Symmetric Case	$U[0.675, 0.825]$	$U[0.45, 0.55]$	$U[3, 7]$
Coanda Case	$U[0.824, 1.007]$	$U[0.30, 0.37]$	$U[3, 7]$

In order to obtain a probabilistic characterization of the different quantities of interest, a PCE can be constructed with the form given in Equation (2).

$$Y^k = \sum_{i=0}^{\infty} c_i^k \phi_i(X_1, X_2, X_3) \approx \sum_{i=0}^{n} c_i^k \phi_i(X_1, X_2, X_3) \qquad (2)$$

In this expression, c_i^k represent the polynomial expansion coefficients, ϕ_i's are orthogonal multivariate polynomials and n is the truncation order of the polynomial expansion. In the present study, the maximum order of the polynomials included in the expansion is 4. Given the uniform distribution of the uncertain parameters, the ϕ_i bases are Legendre polynomials and linear isoprobabilistic transformations are performed to convert the physical domain to the standard domain in [-1,1], and vice versa.

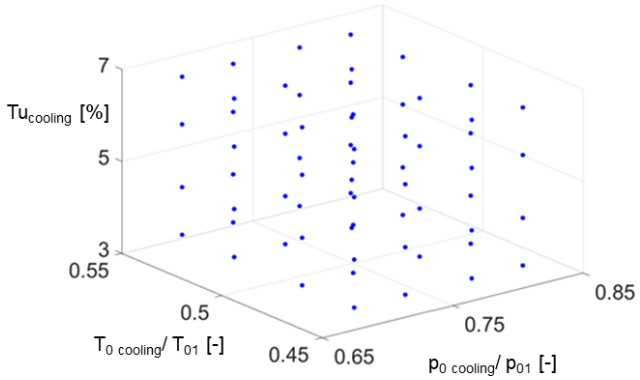

Figure 4: Quadrature points for PCE of symmetric flow topology case.

The PCE coefficients are calculated using the projection approach, which directly follows the PCE definition and the orthogonality conditions of the polynomials. The mathematical

expression giving these coefficients is shown in Equation (3). The integrals given in the definition need to be calculated over the domain wherein the input random variables are defined, i.e., Ω_X. Here, these integrals are calculated numerically using the Gauss quadrature rule on an isotropic tensor grid determined by the zeros of ϕ_i polynomials. The quadrature points are represented by $\left(X_1^j, X_2^j, X_3^j\right)$ and the weights are indicated by w^j where $j = [1, N]$ and N is the total number of points, and consequently, the number of simulations needed to fully define the PCE. For a multi-dimensional tensor-based quadrature, $N = (n+1)^{dim}$ quadrature points are needed in order to perform the numerical integration. Where n is the order of the polynomial expansion considered and dim is the number of input variables considered in the problem. In the present study, $N = (4+1)^3 = 125$ points were required. Hence, 125 two-dimensional RANS simulations for each of the baseline cases considered here were needed.

$$c_i^k = \frac{\int_{\Omega_X} Y^k \phi_i dX_1 dX_2 dX_3}{\int_{\Omega_X} \phi_i \phi_i dX_1 dX_2 dX_3} \approx \frac{\sum_{j=1}^{N} Y^k\left(X_1^j, X_2^j, X_3^j\right)\phi_i\left(X_1^j, X_2^j, X_3^j\right)w^j}{\sum_{j=1}^{N} \phi_i\left(X_1^j, X_2^j, X_3^j\right)\phi_i\left(X_1^j, X_2^j, X_3^j\right)w^j} \quad (3)$$

The constructed PCE serves as the reduced-order model for the statistical analysis of the output quantities of interest. The expected value (E) and variance (V) for the different quantities interest (Y^k) can be obtained from the expansion coefficients as shown in Equations (4) and (5).

$$E[Y^k] = c_0^k \quad (4)$$

$$V[Y^k] = \sum_{i=1}^{n} c_i^k \quad (5)$$

Additionally, the Probability Density Functions of the different quantities of interest, is calculated by taking samples from the constructed PCE.

In order to perform the probabilistic side of the present work, the Matlab-based UQ framework developed at ETH Zurich UQLab [13] was employed. This tool was employed at three stages of the calculation process. Firstly to generate the quadrature points at which the RANS calculations needed to be performed. Once these calculations were post-processed, their output data was fed back to UQLab. At this point of the algorithm, UQLab was used to generate the PCE. Lastly, once the PCE had been computed, UQLab was employed to take samples of them, obtaining this way the probability density functions of the different quantities of interest.

2.4 Pade-Legendre polynomial chaos expansion

The classical polynomial basis introduced above has been developed for the applications with smooth functions. In order to capture the discontinuities appearing in the shock-dominated flows, Chantrasmi et al. [14] proposed the Pade-Legendre polynomial chaos expansion which offers a superior accuracy compared to the classical basis. This expansion is essentially formed as the ratio of two Legendre polynomials series, as shown in Equation (6). In this expression, $\hat{p}_j$ and $\hat{q}_j$ are coefficients of the expansion, while P_j and Q_j are multivariable Legendre polynomials. A given output variable y is approximated by the ratio of both expansions. The values $c(M)$ and $c(L)$ are integer parameters described in [14], together with a detailed explanation on how to calculate the polynomial expansion coefficients. Once the quantities of interest are expressed in a compact form as a function of the polynomial expansion, these expressions can be used to take samples and identify their probabilistic data such as moments, probability density function and confidence interval bounds.

$$y \approx \frac{\sum_{j=1}^{c(M)} \hat{p}_j P_j(X_1, X_2, X_3)}{\sum_{j=1}^{c(L)} \hat{q}_j Q_j(X_1, X_2, X_3)} \quad (6)$$

2.5 Sobol indices for sensitivity analysis

Sobol index is a quantitative measure to estimate the sensitivity of an output to a set of inputs [15]. This methodology is based on decomposing the variance of a given output ($V[Y^k]$) to the contributions from each individual input variable as well as their interactions, following Equation (7):

$$V[Y^k] = \sum_{i=1}^{n_X} V_i + \sum_{i<j}^{n_X} V_{ij} + \cdots + V_{12\ldots n_X} \quad (7)$$

where the first term on the right-hand side includes the variance of each input variable separately, while the second summation incorporates the second and higher-order interactions of input variables. Accordingly, the first-order Sobol indices ($S_i^{Y^k}$) are calculated as the ratio of the contribution of a particular input variable (X_i) over the complete variance of the given quantity of interest (Y^k), shown in Equation (8):

$$S_i^{Y^k} = \frac{V_i^{Y^k}}{V[Y^k]} \quad (8)$$

and higher-order Sobol indices, e.g., $S_{ij}^{Y^k}$, measure the importance of the interaction between different input variables on the outputs.

3. Results and discussion

3.1. Symmetric flow topology characterization

Figure 5 presents the *mean* and *standard deviation* of Mach number in the vicinity of the leading edge subjected to the variability of the blowing parameters. The mean Mach number contour, Figure 5 (a) the same supersonic injection flow topology already discussed in Figure 2 (b). From left to right, the first notable feature is the bow shock, separating the free stream from the more complex phenomena taking place near the leading-edge injection. Thereafter, another curved region with a sharp gradient is found that separates "supersonic Mach numbers" from the "low subsonic ones". The saddle point is located in this low subsonic region which appears right upstream of the supersonic region as the leading-edge jet expands upon leaving the injection cavity. Both regions are separated by the terminal shock.

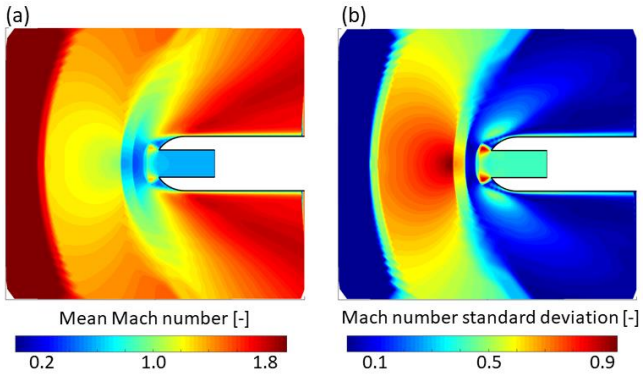

Figure 5: Symmetric flow topology leading edge Mach number contours obtained from PCE: Mean value (a) and standard deviation (b).

On both sides of the leading-edge, the two low-momentum separation zones can be identified, typical of a supersonic injection. Right downstream the separation bubble, an expansion fan accelerates the flow, a characteristic feature of both subsonic and supersonic injections, as observed in Figure 2.The standard deviation of Mach number near the leading-edge with stochastic injection parameters is illustrated in Figure 5 (b). The results suggest that the highest variations in the leading-edge flow topology occur between the bow shock and the saddle point, together with the expansion region appearing at the exit of the injection cavity. Different injection conditions, generated by the stochastic boundary conditions, impose different momentum boundary conditions at the injection cavity which, in turn, pushes the standard flow pattern to different distances upstream the leading edges. Furthermore, different leading-edge jet characteristics result in a change in the size of some upstream features, like the supersonic pockets appearing right upstream the injection cavity. Higher values of cooling total pressure lead to higher momentum and if the injection is supersonic, they induce a higher size of that supersonic area at the cooling cavity exit.

The two recirculation areas on the sides of the injection port are also characterized by large variability in their Mach number, see their bright blue or green color in the standard deviation map in Figure 5 (b). However, the magnitude of such variation is significantly less than the levels observed in the supersonic expansion region right upstream of the injection cavity or between the saddle point and the bow shock position. These two last regions are characterized by red color in the map in Figure 5 (b).

The results obtained from the PCE for the wall variables on the airfoil's surface are presented in Figure 6. This includes the static pressure normalized by the inlet total pressure (a), skin friction coefficient (b) and Nusselt number (c). The skin friction coefficient was obtained by normalizing the wall shear stress by the inlet dynamic pressure, as given in Equation 9. The Nusselt number was calculated based on the leading edge diameter and the local heat transfer coefficient as given in Equation 10. While the local heat transfer coefficient was computed considering the inlet total temperature as the driving mechanism for heat transfer, as shown in Equation 11. In Figure 6 (a)-(c), the mean value is given by a solid line, while 95 % confidence intervals are represented by a shaded area bounded by dash-dotted lines. Moreover, for each variable, an example of a subsonic (green) and a supersonic (magenta) injection are given by two dashed lines.

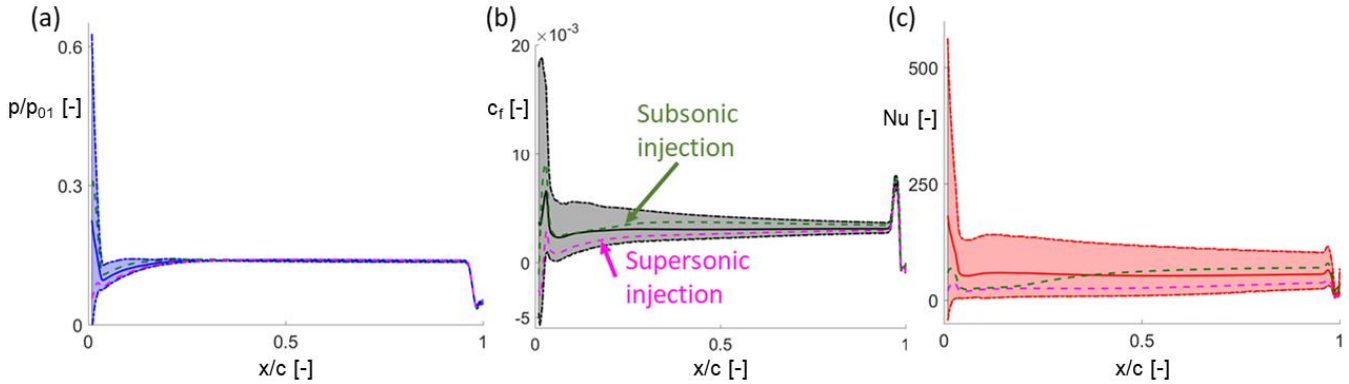

Figure 6: Distribution of wall quantities on the airfoil surface, for the symmetric flow topology, taken from PCE: Normalized static pressure (a), skin friction coefficient (b) and Nusselt number (c). Solid lines denote mean value distributions. The shaded regions

denote 95 % confidence intervals and the green and magenta dashed lines represent two sample realizations for the subsonic and supersonic injection regimes.

$$c_f = \frac{\tau_w}{\frac{1}{2}\rho_1 u_1^2} \quad (9)$$

$$Nu = \frac{hd}{k} \quad (10)$$

$$h = \frac{q}{T_{01} - T_w} \quad (11)$$

The mean distribution of static pressure on the wall, shown in Figure 6 (a), indicates that the highest value occurs near the leading-edge. As the flow moves downstream, it expands, decreasing the static pressure, until this variable reaches a plateau. Finally, it goes through a sudden drop at the trailing edge vicinity, where it enters the base region. Regarding the confidence interval, the maximum impact of the uncertainty in the leading-edge injection conditions is observed near the source of uncertainty. This effect on the static pressure quickly decays, being barely noticeable beyond $x/c \approx 0.25$.

The mean wall shear stress distribution, shown by the solid line in Figure 6 (b), features a peak near the leading-edge, before going down to a plateau that covers most of the airfoil. Finally, near the trailing edge, it goes through a sharp peak and falls to negative values due to the boundary layer separation at the base region. The mean distribution is similar to the sample realization for a subsonic injection indicated by the dashed green line. A substantial difference is observed compared to the supersonic injection near the leading-edge where negative values of wall shear stress are reported, as a result of the large separation bubble in this region. These negative values appear as part of the 95 % confidence interval shown in Figure 6 (b). The largest impact of the variations in the leading-edge injection boundary conditions happens at the leading edge. In this case, although the width of the confidence interval decreases, a notable band is maintained throughout most of the airfoil.

For the heat flux distributions shown in Figure 6 (c), the mean distribution exhibits its peak value at the leading edge, and then quickly decays towards a plateau and remains nearly constant afterward up to the trailing edge, where the base region phenomena cause a sudden drop in heat flux. The 95 % confidence interval evolution along the airfoil geometry has similar behavior to that observed for the wall shear stress.

Therefore, the uncertainty in the leading-edge injection condition has a different impact on the static pressure compared to the wall fluxes along the airfoil. Although, in all cases, the largest confidence interval appears at the leading-edge and decays afterward, for the static pressure, this decrease leads to a collapse of all curves, making the influence of the variation in the leading edge injection boundary conditions barely noticeable after $x/c \approx 0.25$. While for the wall shear stress and heat flux, the confidence interval maintains a significant value along most of the airfoil.

The effect of stochastic injection boundary conditions on the bow shock can be analyzed through the Probability Density Function (PDF) of the distance between the leading-edge and the bow shock, shown in Figure 7. The horizontal axis represents this distance, x_{shock}, normalized by the leading edge-diameter, d. The distribution features a mean value of 1.21, while the 95 % confidence interval bounds are 0.28 and 2.13. Therefore, variations at the leading-edge injection conditions can lead to variations as large as ± 75 % in the bow shock position. The pdf is rather uniform near the mean value, featuring two moments on both sides of this center. These two moments are associated with the subsonic and supersonic injection regimes and they accumulate 70 % of the occurrences reflected in the PDF. It should be noted that the mean conditions were chosen at the boundary between both injection regimes.

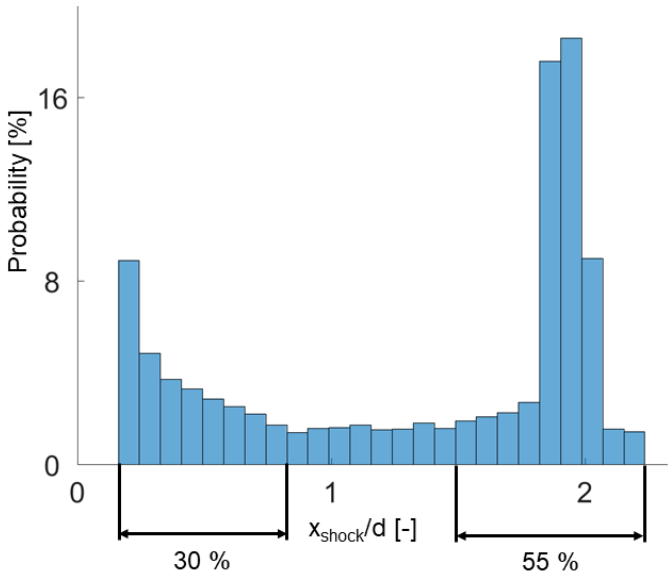

Figure 7: Bow shock stand-off position probability density function for symmetric flow topology case.

In order to determine the influence of the different injection boundary conditions on the output variables, the Sobol indices are analyzed. Figure 8 presents the first-order Sobol indices for the Mach number distribution at the leading-edge vicinity. Plot (a) shows the influence of the cooling total pressure, $S^M_{p_{0c}}$, (b) shows the contribution of the cooling total temperature, $S^M_{T_{0c}}$ and (c) characterizes the impact of cooling turbulence intensity, $S^M_{Tu_c}$ on the Mach number. In Figure 8 (a), it can be observed that the highest influence through most of the domain is from the cooling total pressure, whose Sobol

index is mostly above 0.9. The only exceptions are "near the bow shock" (slightly below $S^M_{p_{0c}} \approx 0.9$) and the two "expansion fans" on both sides of the leading-edge, wherein $S^M_{p_{0c}}$ noticeably decreases, therefore, the impact of Mach number is smaller. The Sobol indices for the total temperature and turbulence intensity *peak* at these expansion regions, revealing a higher influence from those parameters.

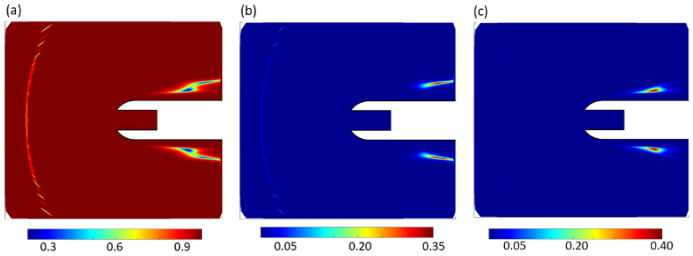

Figure 8: Symmetric flow topology leading edge Mach number first order Sobol's indices: $\boldsymbol{S^M_{p_{0c}}}$ (a), $\boldsymbol{S^M_{T_{0c}}}$ (b) and $\boldsymbol{S^M_{Tu_c}}$ (c).

In this region, the impact of interactions between the uncertain parameters on the Mach number is also examined by visualizing the higher-order Sobol indices at one specific location. This point is indicated in Figure 9 (a) together with the mean Mach number contour, calculated from PCE. Figure 9 (b) presents the contribution of different Sobol indices in the specified location using a pie chart. Regarding the first-order Sobol indices, the turbulence intensity has the highest contribution at this location, followed by the cooling total pressure, while the cooling total temperature has only a minor contribution. Therefore, the turbulent fluctuations coming from the cooling injection have the highest influence on the behavior of the expansion fans happening on both sides of the leading-edge geometry. Interestingly, higher order terms, which indicate interactions among various input variables, have the second highest interaction overall.

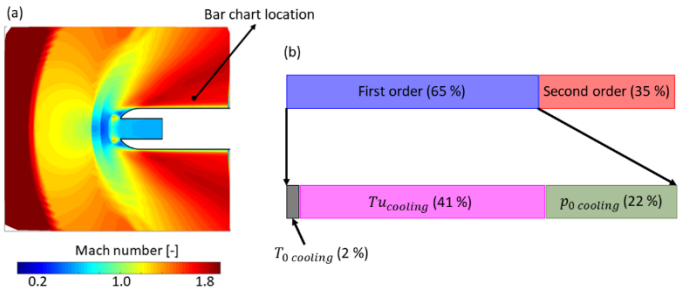

Figure 9: Mean Mach number contour near the leading edge calculated using PCE (a) and Sobol indices pie chart at expansion fan (b).

The next step is to determine which high-order interactions are most influential on the Mach number. Figure 10 represents the contribution of two largest Sobol indices around the leading edge: $S^M_{p_{0c},T_{0c}}$ (a), which describes the effect of interactions between p_{0c} and T_{0c}, and $S^M_{p_{0c},Tu_c}$ (b), which represents the effect of interactions between p_{0c} and Tu_c. These two contours illustrate how the contribution of these second-order Sobol indices is mostly negligible near the leading edge. However, they show a higher influence on the expansion fans on the sides of the leading edge. Hence, the flow pattern in these two regions is influenced by the cooling turbulence intensity as well as $p_{0c} - T_{0c}$ and $p_{0c} - Tu_c$ interactions.

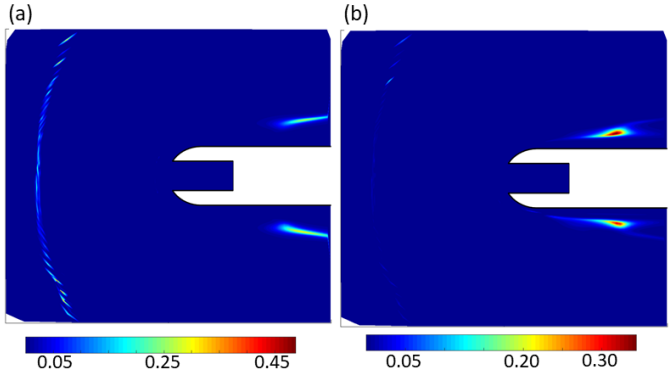

Figure 10: Contours of the second-order Sobol indices on the Mach number for the case with symmetric flow topology: $\boldsymbol{S^M_{p_{0c},T_{0c}}}$ (a) and $\boldsymbol{S^M_{p_{0c},Tu_c}}$ (b).

3.2. Drag reduction and its mechanism

The drag reduction caused by leading-edge injection in the symmetric flow topology case can be observed in Figure 11. It shows the Probability Density Function of the drag obtained for different leading edge injection conditions, normalized by the drag of the airfoil subjected to the same supersonic free stream conditions, without leading-edge injection. This ratio being lower than 1 implies that the drag with the leading-edge injection is lower than without it. The Probability Density Function of drag ratio shown in Figure 11 has a mean value of 0.03, with the 95 % confidence interval bounds at 0.002 and 0.07. Similar to the PDF of the bow shock position (see Figure 7), two peaks are observed: the one at the lower tail is associated with supersonic injection, while the one at the higher tail corresponds to subsonic injection cases. This behavior is due to the fact that the larger momentum injected by the leading edge jet for supersonic injection leads to larger drag reductions than those obtained for subsonic injection.

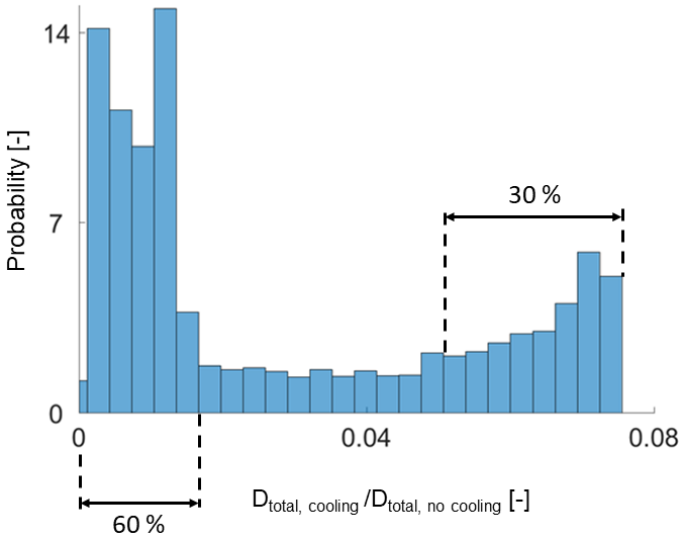

Figure 11: Probability Density Function of drag reduction in the case with symmetric flow topology.

In order to gain further understanding of the physical mechanism causing the drag reduction via the leading-edge injection, the near-wall flow field has been analyzed at several locations around the airfoil. Figure 12 (a) shows the sketch of the airfoil geometry, with a large leading-edge injection slot, together with the lines along which the flow profiles were extracted. Four different profiles were chosen to be analyzed. Three of them are located at the leading edge, at 45, 67.5 and 90° of inclination with respect to the geometry symmetry line.

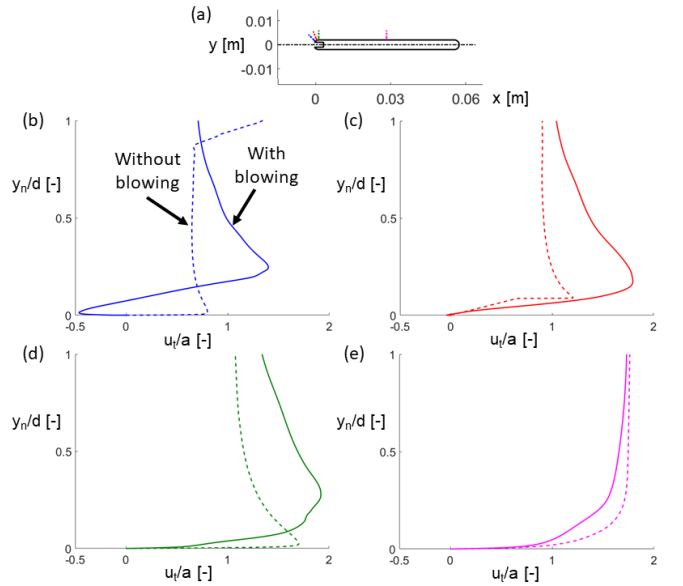

Figure 12: Profiles locations along which data was extracted sketched with airfoil geometry (a); normalized velocity profiles tangential to the airfoil geometry with (solid lines) and without (dashed lines) leading edge injection: at $\mathbf{45°}$ (b), $\mathbf{67.5°}$ (c) and $\mathbf{90°}$ (d) around the leading edge and at mid-chord (e). Data obtained from the case at $\boldsymbol{p_{0\,cooling}/p_{01} = 0.818}$, $\boldsymbol{T_{0\,cooling}/T_{01} = 0.527}$ and $\boldsymbol{Tu_{cooling} = 5\,\%}$.

Figure 12 (b)-(e) presents velocity profiles along these four lines following the same color schemes used in Figure 12 (a). The solid lines correspond to the case with leading edge injection, while dashed lines correspond to a case with no leading edge injection. In both cases, the data was obtained from the steady RANS simulations. For the case with leading edge injection, the blowing total pressure and temperature ratios were 0.818 and 0.527, respectively and the blowing turbulence intensity was $Tu_{cooling} = 5\,\%$. The velocity depicted is tangential to the local airfoil geometry u_t, thus perpendicular to the lines along which the data was extracted, and it is normalized by the local speed of sound a. The wall-normal distance, y_n, is normalized by the leading-edge diameter. In Figure 12 (b), the profiles at 45° are depicted. A small region of separated flow, i.e., negative u_t, is observed for the case with the injection, since this profile is inside the separation region appearing near the leading edge subjected to the supersonic injection. For the profile at 45° without injection, near $y_n/d = 1$, a sharp jump in velocity is observed. This is due to the bow shock, which causes a sharp decrease in velocity from the free stream to the leading-edge vicinity. Overall, the profiles shown in Figure 12 (b)-(d) have larger gradients near the wall for the case with the leading-edge injection, compared to the case without it. Therefore, the leading-edge injection creates an increase in momentum, which is responsible for the drag reduction found. This effect is decaying along the blade's surface and even reversed further downstream from the leading edge. The velocity profile at mid-chord shown in Figure 12 (e) suggests that wall shear stress in the case with injection is smaller. Therefore, in this region where the frictional drag is the dominant component, the leading-edge blowing effectively reduces the drag.

3.3. Coanda effect cases analysis

This section focuses on the cases wherein the stochastic leading-edge injection conditions lead to a non-symmetric flow pattern, namely the Coanda baseline, characterized by a narrow injection slot. Figure 13(a) presents the mean Mach number contour near the leading-edge obtained from the PCE and Figure 13(b) indicates the coefficient of variation, i.e., the ratio of standard deviation over mean value, for the same flow quantity. The emergence of the Coanda effect for certain cases makes the mean flow topology appear non-symmetric. In this mean flow field, the Coanda effect causes the leading-edge jet to deflect to one side, making the sizes of the two recirculation regions on the jet sides non-equal. One recirculation bubble grows larger, pushing the jet to the opposite side, as it has been documented for other cases with non-symmetric flow topology occurring for sudden expansions, see e.g. [11][12] [16]. It has even been used for flow control purposes at the base region of airfoil geometries [16][17]. The cooling jet observed in the mean Mach number contour corresponds to a subsonic injection which expands to the supersonic conditions. This can be seen as the red-colored pocket in between the two recirculation areas as it deflects towards the bottom. Upstream

of this jet, a subsonic region is placed, which occurs as a consequence of flow deceleration across the bow shock located further upstream. This subsonic flow region also contains the saddle point where the mainstream and the leading-edge jet collide.

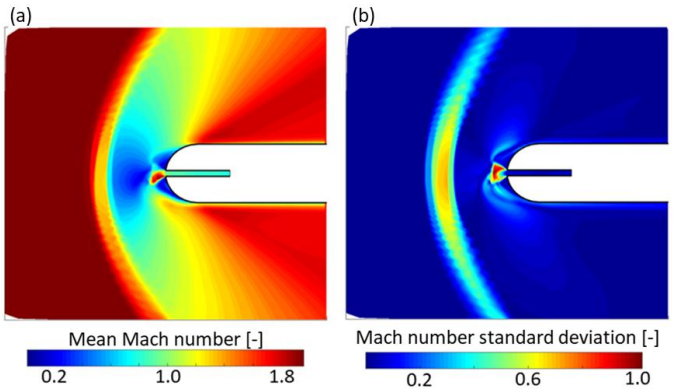

Figure 13: Statistical properties of the Mach number in the Coanda case obtained from PCE: Mean value (a) and standard deviation (b).

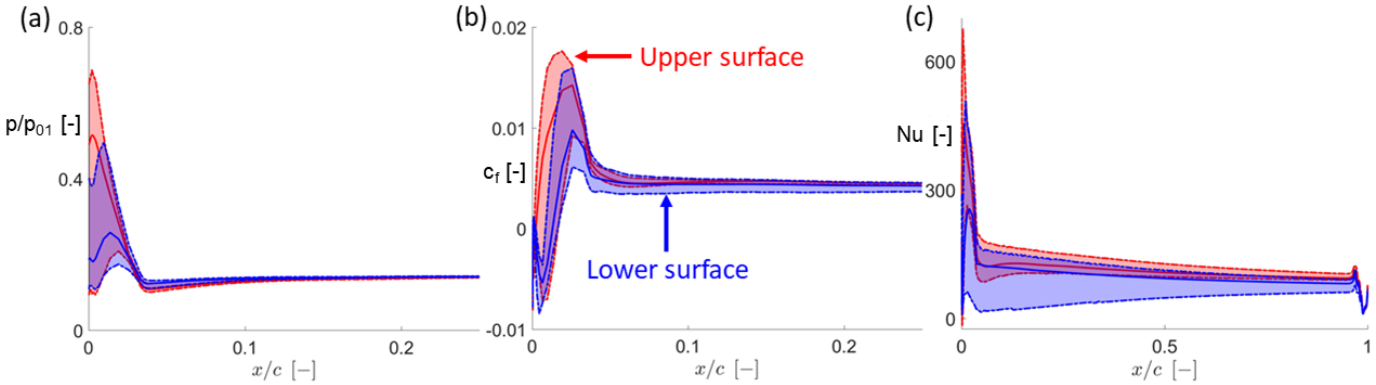

Figure 14: Distribution of normalized static pressure (a) and skin friction coefficient (b) along the airfoil walls near the leading edge, as well as, the profile of Nusselt number along the entire airfoil walls (c): mean values and 95 % confidence interval bounds from PCE, for the Coanda flow topology case.

Mach number's coefficient of variation contour, Figure 13 (b), highlights two main regions of variation, namely the "immediate vicinity of the injection slot" and the "area surrounding the bow shock". The former can be directly associated with the variation between the symmetric and non-symmetric flow topologies, which substantially changes the flow field at that precise location. These two distinct flow topologies, i.e., the symmetric and non-symmetric patterns, also imply a change in the momentum ejected at the leading edge. The axial jet is characterized by a higher momentum which consequently pushes the bow shock further upstream, compared to the non-symmetric one. This explains the variability in the Mach number found near the bow shock position, which is due to alterations in the bow shock position itself. It is noteworthy that at the injection slot exit, the coefficient of variation reaches values exceeding 1.4, meaning that the standard deviation of Mach number at this location is more than 40 % larger than the mean Mach number.

Figure 14 represents the distribution of wall variables distributions along the airfoil surface. Plot (a) shows the static pressure normalized by the inlet total pressure, and plots (b) and (c) present the skin friction coefficient and the Nusselt number. Due to the lack of symmetry in the results presented, two sets of curves are presented in each graph. The blue curves represent the wall quantities along the lower airfoil surface, see the sketch in Figure 12 (a), while the red ones correspond to the upper surface. The solid lines describe the mean values, while the shaded region marks the 95 % confidence interval bounds. In all three graphics, on the horizontal axis, the axial distance x is normalized with respect to the airfoil's chord c. For the first two quantities, $p/p_{01}$and c_f, only the region near the leading-edge vicinity is shown since, in further downstream locations, all profiles almost exactly follow the mean values, and the distribution of these mean quantities is similar to that already described for Figure 6 (a) and (b).

The three plots shown in Figure 14 (a), (b) and (c) feature two distinct behaviors occurring on the upper and lower surfaces of the airfoil. Analyzing the distribution of the mean values one can see that the flow characteristics on the upper wall (red) follows the expected trend from an airfoil without leading edge injection [7], with the maximum values in static pressure and Nusselt number appearing at the leading edge, followed by a rapid descend towards a plateau. The wall shear

stress starts from 0 at the leading edge and reaches the maximum value before it plateaus and remains constant until near the trailing-edge. The evolution of mean values on the lower surface (blue), however, share similarities with the supersonic injection case [7], where the static pressure and Nusselt number are significantly reduced at the leading edge, and an area with negative skin friction coefficients appears at the leading edge which corresponds to the separation region neighboring the leading edge jet.

For the three variables examined, namely p/p_{01}, c_f and Nu, their maximum variations occur near the leading edge, where the source of uncertainty is located, i.e., the injection boundary conditions. However, for the first two variables, the width of the confidence intervals rapidly decreases after the leading edge, with their bounds collapsing with the mean values. While for the Nusselt number, the width of the confidence intervals remains significant throughout the airfoil. Therefore, the airfoil's thermal performance is more affected by variations in the leading-edge injection boundary conditions, compared to the aerodynamic performance.

The first-order Sobol indices for the Mach number in the vicinity of the leading edge are presented in Figure 15. Plot (a) illustrates the indices corresponding to the total pressure and plot (b) describes the one associated with the cooling total temperature. The index representing the effect of turbulence intensity is not presented here, since its contribution in this region is found negligible compared to the other two parameters. With the $S^M_{p_{0c}}$ values close to 0.9 throughout a significant part of the leading-edge region, the effect of total pressure on the Mach number variations is dominant. However, this does not hold in certain areas, like the injection slot exit, the vicinity of the bow shock and the fan expansions on both sides of the leading-edge, especially on the upper surface of the blade. In these regions, the contribution of the total temperature is more pronounced, as seen in Figure 15 (b). Higher-order effect is the component influencing the Mach number variations in these areas. This fact can be observed in the contour of the second-order Sobol index in Figure 16. The coupling between p_{0c} and T_{0c} shows indeed high values, even close to 1, especially near the bow shock and the fan expansion over the upper surface of the airfoil, introducing this process as the dominant factor in shaping the flow pattern at those two locations. Other second order Sobol indices, coming from the interaction of the cooling turbulence intensity with other boundary conditions are found to have a negligible impact on the Mach number field.

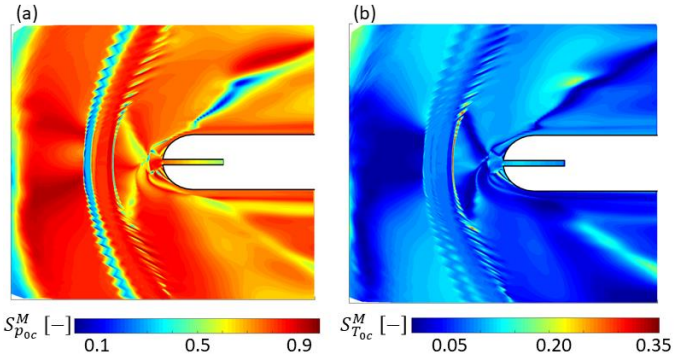

Figure 15: First order Sobol indices for the contribution of total pressure and temperature on the Mach number in the Coanda case: $\boldsymbol{S^M_{p_{0c}}}$ (a) and $\boldsymbol{S^M_{T_{0c}}}$ (b).

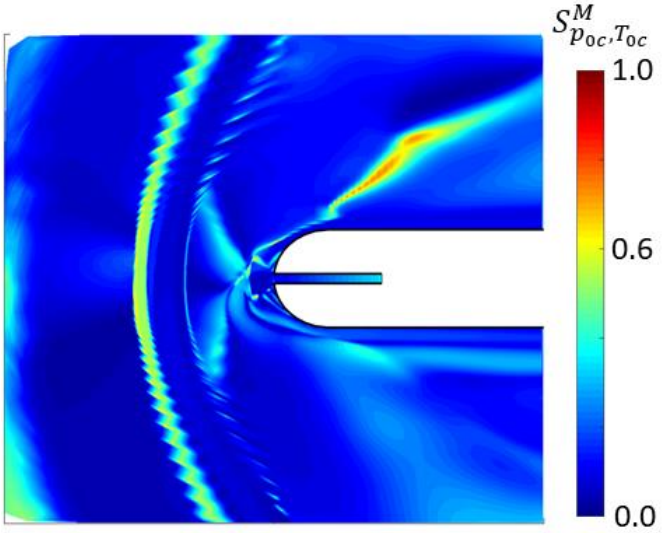

Figure 16: The second-order Sobol index $\boldsymbol{S^M_{p_{0c},T_{0c}}}$ for the Coanda case.

The significant variability in the Mach number near the bow shock implies considerable changes in the position of this feature under the stochastic injection conditions at the leading edge. Figure 17 shows the Probability Density Function of this bow shock's position. Similar to Figure 7, the bow shock's distance from the leading edge is normalized by the leading-edge's diameter d and is shown on the horizontal axis. The distribution features a bimodal behavior, with the first peak at $\Delta x_{shock}/d \approx 0.9$ and the second one at $\Delta x_{shock}/d \approx 1.2$. The first peak is related to the non-symmetric flow topologies, while the second one is associated with symmetric ones. The mean value of the distribution is $\Delta x_{shock}/d = 1.01$, with the 95 % confidence intervals at $\Delta x_{shock}/d = 0.82$ and $\Delta x_{shock}/d = 1.26$.

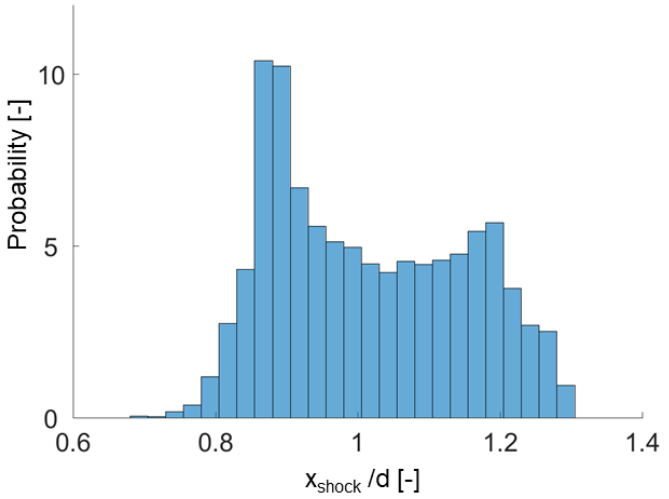

Figure 17: The histogram of the bow shock's distance from the leading-edge (normalized by the leading-edge's diameter) obtained from PCE for the Coanda case.

Two main features distinguish the PDF of the bow shock's position in the Coanda case (in Figure 17) from the one reported for the larger injection slot (in Figure 7). First is the mean value; the larger injection slot adds a higher momentum at the leading edge which pushes the bow shock further upstream. Second, the case with the Coanda flow topologies shows a smaller spread of the Probability Density Function, even though a larger range of variability on the injection boundary conditions was considered. Therefore, for this case, the location of the bow shock is more robust when subjected to stochastic boundary conditions at the leading-edge, compared to the case with the larger injection slot.

3.4. Different polynomial expansions comparison

As part of the present study, the classical PCE approach used throughout this manuscript was compared against the Pade-Legendre basis proposed by Chantrasmi et al. [14] for the discontinuity-dominated flows.

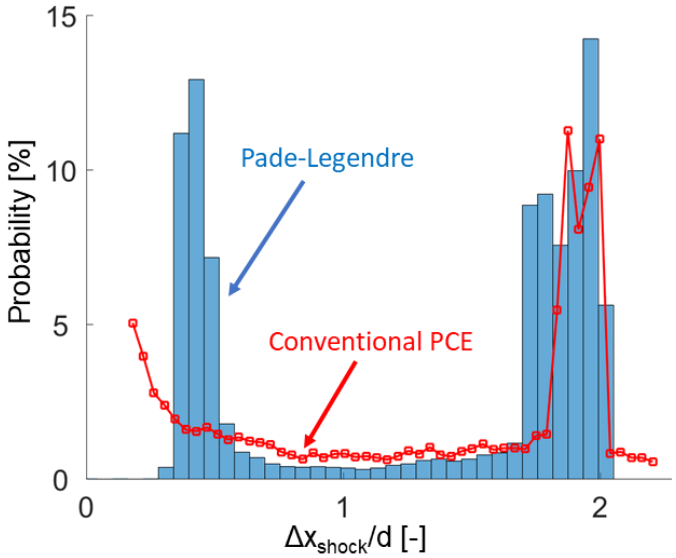

Figure 18: The histogram of normalized bow shock's distance from the leading-edge obtained from Pade-Legendre (blue bars) and conventional PCE (red squares) for the symmetric case.

Figure 18 shows the histogram for the bow shock position (normalized by the leading-edge diameter) obtained from the Pade-Legendre PCE (blue bars) for the symmetric flow topology case, together with the one obtained from the conventional PCE (red squares curve). Both probability density functions show the same behavior, with two peaks appearing at low and high bow shock distances from the leading edge. The lower one is due to the subsonic injection regime, while the upper one corresponds to the supersonic injection. This agreement in the predicted PDF by the conventional and more elaborated PCE ensures the validity of the results obtained with the conventional PCE and the analysis throughout this complete manuscript.

4. Conclusions

The present manuscript investigates the stochastic boundary conditions at the injection port of a counter-flowing jet at the leading edge of an airfoil exposed to a supersonic flow at Mach 2. It is the for first time in the literature that the robustness of such a flow control technique is analyzed and the uncertainties in the flow topology and the aero-thermal performance are characterized. Two different injection sizes are explored: the large slot injection featuring symmetric flow topologies and the small one including non-symmetric flow patterns at certain injection conditions. The boundary conditions considered as stochastic are the total pressure, total temperature, and the turbulent intensity that are assumed to be uniformly distributed.

The largest effect of the stochastic injection boundary conditions on the flow topology is observed right at the exit of the injection as well as near the bow shock. For both injection port sizes analyzed, the Probability Density Functions of the

bow shock positions featured two peaks. In the case of the large injection slot, these two peaks are related to the appearance of subsonic and supersonic injection regimes. In the cases with the small injection slot, these peaks are associated with the appearance of symmetric and non-symmetric flow topologies.

The confidence intervals reported for the wall variables along the airfoil geometry show that the influence of variations in the injection boundary conditions is maximum near the leading-edge. This influence decays with the axial position along the airfoil in all cases. Analysis of Sobol indices reveals the dominance of the cooling injection's total pressure in determining the key flow properties among all the uncertain parameters. Only when it comes to the flow topology, in some areas the cooling injection total temperature, turbulence intensity or higher-order combinations of the uncertain variables feature a larger influence. This is the case for the expansion fans occurring on both sides of the leading edge and the bow shock region for the case with the small injection slot. Hence, in future studies of this configuration, considering only the blowing total pressure would provide good first approximation of the flow response to the stochastic injection conditions.

Acknowledgments

The authors would like to acknowledge "La Caixa" Foundation for supporting this research with Grant No. LCF/BQ/AA17/11610006 through their Postgraduate in North America and Asia-Pacific Programme. GL gratefully acknowledges the support of the National Science Foundation (DMS-2053746 and DMS-2134209) and U.S. Department of Energy Advanced Scientific Computing Research program DE-SC0021142.

Competing interests

The authors declare no competing interests.

Nomenclature

Symbol	Meaning [units]
α	Flow angle [deg]
c	Chord [m]
c_f	Skin friction coefficient [-]
d	Leading edge diameter [m]
D	Drag force per unit length [N/m]
h	Heat transfer coefficient [kW/m^{2}K]
M	Mach number [-]
Nu	Nusselt number [-]
p	Pressure [Pa]
q	Heat flux [W/m^2]
Q	Thermal load [W/m]
t	Time [s]
T	Temperature [K]
Tu	Turbulence intensity [%]
u	Flow velocity [m/s]
ρ	Density [kg/m^3]

Subscripts

0	Total conditions
1	Inlet conditions
2	Outlet conditions
c	Cooling injection conditions

References

[1] Delery, J. & Dussauge, J.P. "Some physical aspects of shock wave/boundary layer interactions". *Shock Waves* **19**, 453-468, https://doi.org/10.1007/s00193-009-0220-z (2009).

[2] Finley, P.J. "The flow of a jet from a body opposing a supersonic free stream". *Journal of Fluid Mechanics* **26**, 337-368, https://doi.org/10.1017/S0022112066001277 (1966).

[3] Bushnell, D.M. "Shock wave drag reduction". *Annual Review of Fluid Mechanics* **36**, 81-96, https://doi.org/10.1146/annurev.fluid.36.050802.122110 (2004).

[4] Najm, H.N. "Uncertainty quantification and polynomial chaos techniques in computational fluid dynamics". *Annual Review of Fluid Mechanics* **41**, 35-52, https://doi.org/10.1146/annurev.fluid.010908.165248 (2009).

[5] Knio, O.M. & Le Maitre, O.P. "Uncertainty propagation in CFD using polynomial chaos decomposition". *Fluid Dynamics Research* **38**, 616-640, https://doi.org/10.1016/j.fluiddyn.2005.12.003 (2006).

[6] Ahlfeld, R., Montomoli, F., Carnevale, M. & Salvadori, S. "Autonomous uncertainty quantification for discontinuous models using multivariate Pade approximations". *Journal of Turbomachinery* **140**, https://doi.org/10.1115/1.4038826 (2018).

[7] Lozano, F. & Paniagua, G. "Airfoil leading edge blowing to control bow shock waves". *Scientific Reports* **10**, https://doi.org/10.1038/s41598-020-79048-w (2020).

[8] Celik, I.B., Ghia, U., Roache, P.J., Fritas, C.J., Coleman, H. & Raad, P.E. "Procedure for estimation and reporting of uncerainty due to discretization in CFD applications". *Journal of Fluids Engineering* **130**, https://doi.org/10.1115/1.2960953 (2008).

[9] Saracoglu, B.H., Paniagua, G., Sanchez, J. & Rambaud, P. "Effects of blunt triling edge flow discharge in supersonic regime". *Computers and Fluids* **88**, 200-209, https://doi.org/10.1016/j.compfluid.2013.09.013 (2013).

[10] Martinez-Cava, A., Wang, Y., de Vicente, J. & Valero, E. "Pressure bifurcation phenomenon on supersonic blowing trailing edges". *AIAA Journal* **57**, 153-164, https://doi.org/10.2514/1.J057056 (2019).

[11] Fearn, R.M., Mullin, T. & Cliffe, K.A. "Nonlinear flow phenomena in a symmetric sudden expansion". *Journal of*

Fluid Mechanics **211**, 595-608, https://doi.org/.1017/50022112090001707 (1990).
[12] Escudier, M.P., Oliveira, P.J. & Poole, R.J. "Turbulent flow through a plane sudden expansion of modest aspect ratio". *Physics of Fluids* **14**, 3641-3654, https://doi.org/10.1063/1.1504711 (2002).
[13] Marelli, S. & Sudret, B. "UQLab: A framework for uncertainty quantification in Matlab". *2nd Inernational Conference on Vulnerability, Risk Analysis and Management*, https://doi.org/10.1061/9780784413609.257 (2014).
[14] Chantrasmi, T., Doostan, A. & Iaccarino, G. "Pade-Legendre approximants for uncertainty analysis with discontinuous response surfaces". *Journal of Computational Physics* **228**, 7159-7180, https://doi.org/10.1016/j.jcp.2009.06.024 (2009).
[15] Sobol, I.M. "Sensitivity analysis for nonlinear mathematical models". *Mathematical Modeling and Computational Experiment* **1**, 407-414, https://doi.org/ (1993).
[16] Saracoglu, B.H., Paniagua, G., Sanchez, J. & Rambaud, P. "Effects of blunt trailing edge flow discharge in supersonic regime". *Computers and Fluids* **88**, 200-209, https://doi.org/10.1016/j.compfluid.2013.09.013 (2013).
[17] Lozano, F., Saavedra, J., Fisher, J., Paniagua, G., Martinez-Cava, A. & Valero, E. "Experimental approach to characterize base region Coanda flow topology induced by pulsating blowing". *8th European Conference for Aeronautics and Space Sciences (EUCASS)*, https://doi.org/10.13009/EUCASS2019-762 (2019).